Strong Polarity-Inversion Line Preceding an X-Class Flare

D.M. Volobuev

Pulkovo Observatory, St.-Petersburg, Russia

dmitry.volobuev@mail.ru

Abstract. The polarity inversion line crossing the bipolar magnetic active region (AR) is known to be one of the most important features to analyze the evolution of solar photospheric magnetic fields and predict solar flares and coronal mass ejection (CME). Here we present efficient algorithm for identification of strong polarity-inversion line (SPIL) on the *Solar Dynamic Observatory* (SDO) *Helioseismic and Magnetic Imager* (HMI) magnetograms. The algorithm is a pixel-level nearest neighbor analyzer based on the cellular-automata approach. Evolution of identified SPIL (100 Gauss threshold) for sequence of magnetograms for AR 11158 shows that the merging of SPIL from relatively small discrete parts to more continues line occurs during 8 hours preceding X-class flare. The algorithm runs on an ordinary PC and lasts only 12 s for the central part of solar magnetogram (2700 × 2700 pixels). We calculated average magnetic field across SPIL with region-growing approach and found that it is smooth analytical function of distance independent of time.

Keywords: Flare forecast, polarity-inversion line, cellular-automata

1. Introduction

Development of methods for predicting strong sunspot flares is important both for improved forecasting of space weather and because it is a way to improve our physical understanding of these magnetic explosions on the Sun. Magnetic field lines snap to a lower energy configuration via reconnection, the excess energy released produces coronal mass ejections (CMEs) and solar flares (e.g., Shibata, 1998; Wang et al.2002; Priest and Forbes, 2002). Emerging flux and non-potential energy which is stored in the magnetic fields play an important role in driving flares (e.g. Gary et al, 1987; Moore and Sterling 2001; Sterling, Harra and Moor, 2007). Despite of very complicated physics of the phenomena of solar flare and CME there are two main features only which are directly observable from regularly measured line-of-sight magnetograms. These are (i) polarity-inversion line which separates patches of positive and negative magnetic flux (e.g. Falconer et al., 2008; Cui et al., 2006, 2007) and (ii) patches of very strong magnetic flux which are proxies for magnetic charge topology (MCT) algorithms (e.g.

Gorbachev and Somov, 1988; Barnes, Longscope and Leka, 2005). Significant progress achieved during recent years in both these directions leads to four most-developed automatic prediction methods which were statistically tested by Barnes and Leka (2008). They showed that the performance of different predictors with respect to major flare daily forecasting is quite similar; all four are strongly correlated with each other (correlation $0.78 \leq r \leq 0.93$). On the other hand they concluded that "The highest success rate for any single parameters was 92.2%, yet this is only a slight improvement compared to the success rate of 90.8% obtained by forecasting that no region will ever produce an M-class or larger flare." This conclusion confirm their previous detailed study of three active regions vector magnetograms (Leka and Barnes, 2003a) where no regular variation of parameters was found with the transition from quiet to flaring conditions, although Leka and Barnes (2003b) also showed that some classifiers (e.g. discriminant analysis) could help. This means that there is still no good predictor for M-class and X-class flares and better algorithms and data are needed.

In this study we found that high-resolution and low-noise SDO line-of-sight magnetograms allow direct identification of SPILs, which uses only logical rule and sorting (neither smoothing nor filtering) of initial data. While preserving the initial data, the algorithm (Section 2) provides the possibility to derive a better flare predictor because a similar algorithm applied to SOHO magnetogram requires smoothing and filtering procedures for SPIL identification (Schrijver, 2007, Wang and Zhang, 2008). Two calculated parameters of SPIL show significant variation with transition from quiet to pre-flare conditions (Section 3). Using region-growing approach with seeds on SPIL we calculated the average shape of magnetic field variation across the SPIL and show that average gradient across SPIL is similar for quiet and pre-flare conditions (Section 4), while most variable is morphological length per continues object of SPIL.

2. Algorithm for SPIL identification

Let us consider the pixel of SDO magnetogram (Figure 1, black square) surrounded by its 8 neighbours (white squares) which is an initial statement for 8-connected cellular automata (Moor neighborhood).

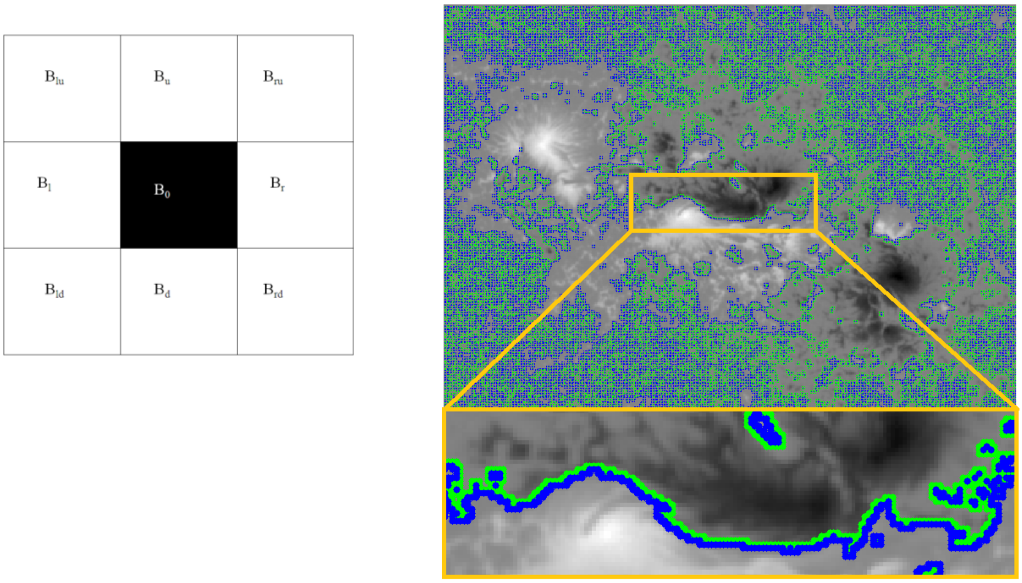

Figure 1. Left panel: Eight-connected pixel with its neighbors. Right panel: Example of polarity-inversion line (PIL) with zero threshold. SDO magnetogram is shown for AR 11158 14 February 2011 at 11:00:00. Blue and green colors show neighboring pixels of negative and positive polarity.

This pixel has the prescribed magnetic field B_0, with surrounding edge neighbors have B_u, B_d, B_l, B_{r} and vertex neighbors have B_{lu}, B_{ld}, B_{ru}, B_{rd} fields. The pixel B_0 belongs to PIL's positive boundary if $B_0 > \varepsilon$ whereas at least one of its neighbors is essentially negative $B_i < -\varepsilon$ and belongs to PIL's negative boundary:

$$PIL_+ \equiv \bigcup_{B_0 \in M} \left((B_0 > \varepsilon) \bigcap (N(B_0) < -\varepsilon) \right)$$

$$PIL_- \equiv \bigcup_{B_0 \in M} \left((B_0 < -\varepsilon) \bigcap (N(B_0) > \varepsilon) \right) \qquad (1)$$

$$PIL \equiv PIL_+ \bigcup PIL_-$$

There $N(B_0)$ is Moor's neighborhood of pixel B_0, M is a magnetogram set of pixels. Logical rule (1) reveals the PIL (Figure 1, Right panel) even with zero threshold [ε=0].

According to the definition (1) the PIL has a two-pixel width**; difference between diagonal and non-diagonal pixels is neglected.** Theoretically PIL should be a line between the pixels, because it should belong to neither positive nor negative magnetic polarity. Empirically a finite-width PIL (1) is more convenient and informative because it contains boundary pixels of both magnetic polarities and information about the gradient of the magnetic field across the PIL. In Figure 1, PIL pixels of negative and positive polarities are indicated in blue and green. PIL is a function of the threshold [ε] by definition. The threshold is chosen as ε = 100

Gauss (143 gauss·Mm^{-1}) in this article. This is a high threshold **(***e.g.* Cui *et al.* (2006) used 41 gauss·Mm^{-1}, **Falconer Moor and Gary (2008) used 50 gauss**·Mm^{-1}**)** so we called this PIL a strong polarity-inversion line or SPIL which corresponds to terminology of Schrijver (2009). **More correctly for digital magnetograms is to compare a gradient flux threshold which is aforementioned threshold multiplied by pixel area. This corresponds to 0.71 x 10^{18} Mx**·Mm^{-1} for **SDO (this article)** ***vs*** **0.89 x 10^{18} Mx**·Mm^{-1} **for SOHO** (**Cui et al., 2006)**. The threshold is an appropriate value, because much smaller ε leads to increasing of noisy discrete pieces of PIL, which do not belong to AR but to the quiet Sun (Figure 1, Right panel). Larger ε leads to larger visible differences between quiet and flaring conditions but also leads to poorer statistics of pixels that belongs to the SPIL (Figure 5). AR 11158 SDO magnetograms analyzed here allow threshold $\varepsilon = 50$ gauss which still provides no pixels in the quiet Sun but a threshold $\varepsilon = 10$ gauss leads to huge number of "contaminant" pixels. We should note that the zero-threshold polarity-inversion line (ZPIL) (Figure 1, Right panel) is a much more informative and independent of threshold by definition. It should be particularly useful for studies of the magnetic network but it is beyond the present research. The presented algorithm runs typically in 12 seconds for the central part of solar magnetogram (2700 × 2700 pixels) on an Intel^{R} Core^{TM} 2 Quad CPU 2.33 GHz. MatLab^{R} code is published at www.matlabcentral.com File ID: #31649. **Algorithm can be adopted for 4-connected automata, it works faster but prescribes a rectangular turns of the PIL.**

3. SPIL Evolution Before X-Class Flare

The gradient weighted inversion line length (GWILL) is an important predictor for strong flares but typically requires an iterative-smoothing procedure for its identification (*e.g.* Mason and Hoeksema, 2010, Martens *et al.*, 2011). GWILL definition grows from the parameter L_{SG}, which was proposed by Falconer, Moore and Gary (2003). **It is identical to parameter WL_{SG} by Falconer, Moore and Gary (2008)**

$$WL_{SG} = \int (\nabla B_z) dl \quad \text{[Gauss]} \qquad \textbf{(2)}$$

where ∇B_z is the horizontal gradient of the vertical magnetic field and integration is along the PIL. Digitizing of this equation leads to

$$WL_{SG} = \sum_i \frac{(B_z^+ - B_z^-)_i}{l_i} l_i = \sum_i (B_z^+ - B_z^-)_i \qquad \textbf{(3)}$$

where B_z^+, B_z^- are positive and negative magnetic fields assigned to neighboring pixels across the PIL defined by Equations (1). Digital magnetogram associates the measured magnetic field with pixel of definite size and shows the changes of magnetic flux rather than the magnetic field in a point. Consequently, we expect that a local magnetic flux

$$\Phi_z = B_z l_0^2 \qquad \textbf{(4)}$$

which is vertical magnetic field multiplied by the pixel area is the better invariant if pixel size changes (e.g. transition from SOHO to SDO magnetogram). Similar to Equation (1) we can introduce the parameter

$$\mathrm{GWILL}_{\Phi} = \int (\nabla \Phi_z) dl \ \ [\mathrm{Maxwell}]. \qquad \textbf{(5)}$$

This parameter will differ from WL_{SG} by the multiplier (pixel area) which can be considered as a constant for the given instrument if projection effect is neglected. Digitizing the definition (5) leads to

$$\mathrm{GWILL}_{\Phi} = \sum_i \frac{(B_z^+ - B_z^-)_i l_i^2}{l_i} l_i = \sum_i (B_z^+ - B_z^-)_i l_i^2 \qquad \textbf{(6)}$$

Mason and Hoeksema (2010) proposed to compute GWILL as

$$\mathrm{GWILL}_{MH} = \sum \nabla B \qquad \textbf{[gauss·Mm}^{-1}\textbf{]} \qquad \textbf{(7)}$$

where the gradient is across PIL whereas the sum is along the PIL. This definition will be computationally equivalent to (4) and (2) if pixel size is equal to one $l_i = 1, \forall i$.

Definition (5) by Mason and Hoeksema (2010) prescribes the dimension unit for GWILL$_{MH}$ to be gauss·Mm^{-1} but they measure GWILL$_{MH}$ in Mm in their Figure 3 which is inconsistent.

We use here definition (6) to calculate GWILL flux. Calculations were done summing B^+ and B^- separately which simplifies the algorithm using an assumption that positive and negative magnetic fluxes are balanced in the vicinity of the SPIL:

$$\mathrm{GWILL}_{\Phi} = \sum_i B_{zi}^{+} l_i^2 - \sum_i B_{zi}^{-} l_i^2 \qquad \textbf{(8)}$$

Basing on Cui et al. (2006) conclusions the projection effect can be ignored for PIL parameters calculated for ARs within 30^o of central meridian. So we

assume here that pixel size does not change significantly for the central part of solar disc and can rewrite Equation 8 as

$$\mathrm{GWILL}_{\Phi} = \left(\sum B_{zi}^{+} - \sum B_{zi}^{-}\right) l_0^{2} \qquad \textbf{(9)}$$

where $l_0^2 = 0.49Mm^2$ **for SDO magnetogram. Positive and negative magnetic fields are summarized separately and then subtracted. In general case projection effect can be taken into account in Equations 3, 6, 8 by appropriate replacing of pixel size** l_i **with longitude and latitude dependent pixel sizes** $l_i^{\theta} = l_0/\cos\theta$ **,** $l_i^{\varphi} = l_0/\cos\varphi$ **, which makes the algorithm more accurate but more sophisticated and time consuming.** Following definition (5), we show in Figure 2 GWILL flux which is measured in Maxwells.

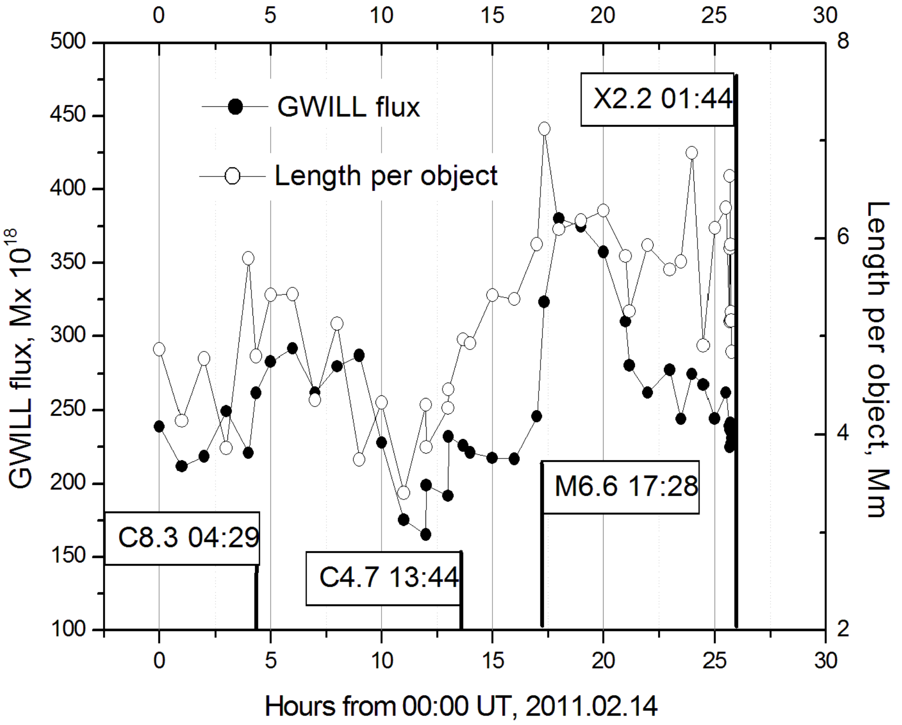

Figure 2. Temporal evolution of SPIL parameters for AR 11158 14 February 00:00UT to 15 February 00:45UT. Flags show C, M, and X-class flares. 11:00 UT and 17:20 UT are chosen as reference times

GWILL flux is similar by its physical sense to parameter *R*, which was proposed by Schrijver (2007), and is a direct measure of the amount of magnetic flux close to a high-gradient polarity-invertion line. It was interpreted by Schrijver (2007) as a proxy for the emergence of current-carrying flux.

Another SPIL parameter which we calculate here is length-per-object, which comes from a morphological analysis of images. Some morphological parameters for ARs on SOHO magnetograms were calculated by Wang and Zhang (2008). SPIL defined by Equation (1) with a strong threshold is not a connected object (Figure 3). It consists of a number of smaller connected objects which we will call subSPILs hereinafter. Here “connected” means that the subSPIL consists of morphologically connected pixels. The mathematical definition of morphological connectivity is discussed, *e.g.* by Serra (1998) and Ronse and Serra (2001) and now this is a part of a powerful non-linear image analysis technique with operators for segmenting, filtering and feature extraction in grey-scale images.

In mathematical morphology, the definition of connectivity comes from the so-called “reconstruction from a marker” procedure: we have an object (SPIL) called the mask, which represents the data to be analyzed, and a set *X* called the marker (a pixel on the SPIL, which is a seed to grow the subSPIL) and we want to obtain all connected components of SPIL which intersect X. The straightforward algorithm for this purpose is to initialize the subSPIL reconstruction with $X \bigcap$ SPIL and to increment it iteratively by adding the neighborhood in subSPIL of each of its pixels

$$\mathrm{subSPIL}_{\mathrm{new}} = \mathrm{subSPIL}_{\mathrm{old}} \bigcup \left(\bigcup_{X \in subSPIL_{old}} \left(N(X) \bigcap SPIL \right) \right) \qquad (10)$$

Here *N(X)* is Moor's neighborhood of *X* (see Figure 1, Left panel). This algorithm is repeated until no further point is added to subSPIL and seeding of markers *X* is continued until no new subSPILs arise.

We show the length per connected object in Figure 2, which is by definition the total length of the discrete SPIL divided by the number of morphologically connected subSPILs. Parameters of the morphological complexity of SPIL were found by Wang and Zhang (2008) most effective for prediction of fast CME. In the case of a SPIL, pixels with small magnetic field are cut by threshold and morphological properties (discreteness) of the SPIL reflect structuring of smaller fields. We can see from Figure 2 that length-per-object is the better predictor in this case compared with GWILL which drops after the M-class flare down to nearly quiet conditions. Parameters shown in Figure 2 grow before a strong flare consistently with typical PIL parameters variation extracted from SOHO magnetogram for strong flares (Mason and Hoeksema, 2010). Figure 3 illustrates the growing of length-per-object parameter as a merging of SPIL which occurs for

AR transition from quiet (left panel) to pre-flare conditions (right panel) and persists until the X-class flare.

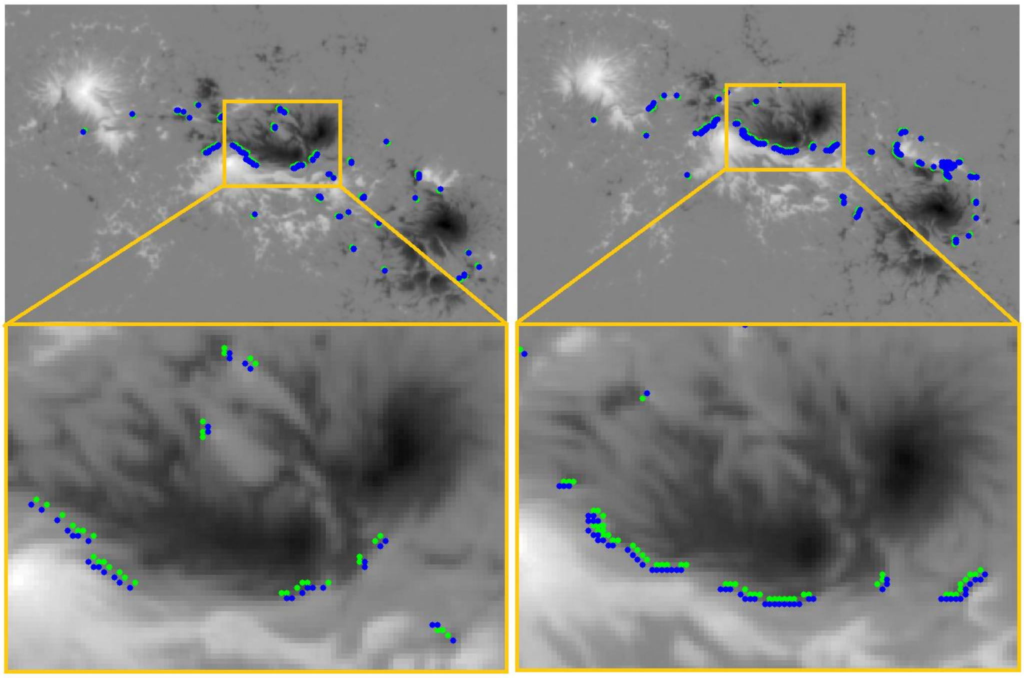

Figure 3. SPIL for AR 11158. Right panel shows magnetogram at 11:00 UT (Quiet conditions) and left panel shows magnetogram at 17:20 UT (pre-flare conditions for M and X–class flares) on 14 February 2011. Blue and green colors show pixels of positive and negative polarity. Bottom inserts show zoomed pieces of SPIL.

4. SPIL Gradient

Gradient of the magnetic field across the SPIL contributes to the GWILL prediction parameter (see Equations 2, 5, 7)**.** This gradient calculated as a function of distance would be also important for MCT-based parameters which use connectivity of magnetic charges through SPIL (*e.g.* Barnes and Leka, 2006; Georgoulis and Rust, 2007) and for general understanding of the physics of a bipolar AR. The complex geometry of a SPIL does not allow direct calculation of how magnetic field grows with distance from polarity-inversion line and we use a region-growing approach (*e.g.* Benkhalil *et al.* 2006; Wang and Zhang, 2008) to identify how the SPIL pixels are connected with regions of high magnetic flux (“magnetic charges”).

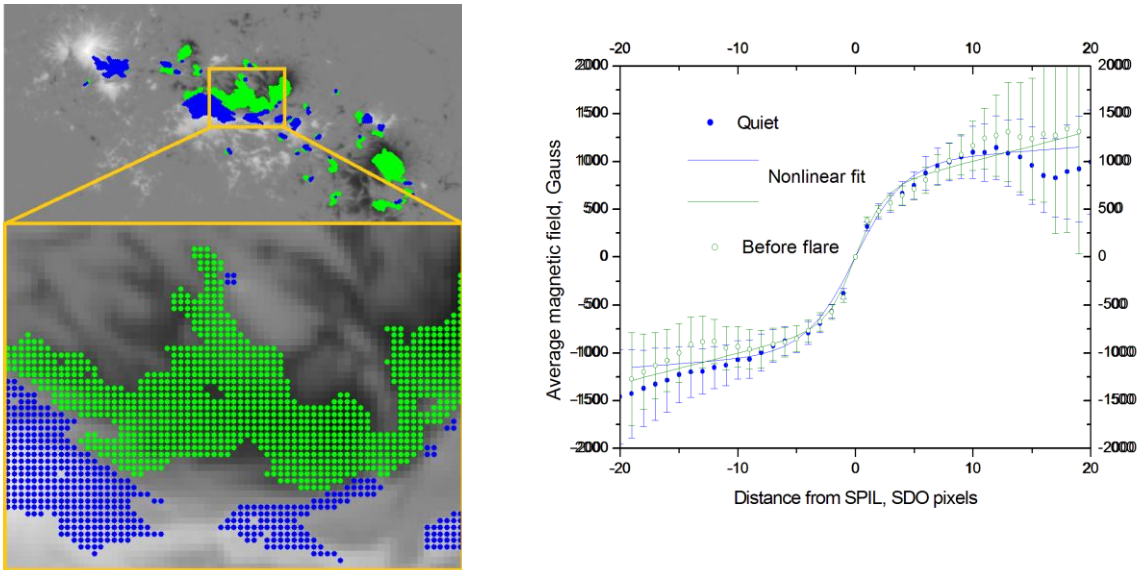

Figure 4. Left panel: SPIL for AR 11158 14 February 2011 11:00UT (Quiet conditions) with regions of strong flux near the SPIL identified with a region-growing algorithm. Blue and green colors show pixels of positive and negative polarity. Right panel: Average magnetic field of growing region as a function of distance from the SPIL, SDO pixel is 0.7 Mm. Nonlinear fit shows the function of Equation (11) for quiet (11:00) and before flare (17:20) conditions. Average is calculated as the mean of an exponential distribution which was fitted to data with 95% confidence interval.

The algorithm consists of three steps: (*i*) seeding the polarity-inversion line, (*ii*) growing the region to nearest neighbor (Figure 1, Left panel) if this neighbor has magnetic flux higher than the seeding pixel which already belongs to the region. (*iii*) Calculate average magnetic field of the pixels attached at this iteration and repeat steps *i* - *iii*, number of iteration corresponds to distance in pixels. Algorithm stops automatically when pixel with maximum magnetic flux is attached to the region. Algorithm is an inversion of standard MCT region mapping, which starts from high fluxes and extends to small. Calculated magnetic field is shown in the right panel of Figure 4 with nonlinear function which fits the data in the least-square sense:

$$B(r) = A \times \tanh(r/B) + C \times r \qquad (11)$$

where A = 986.4 (685.7) gauss is amplitude, B = 4.2 (2.5) SDO pixels is SPIL width and C = 8.6 (31.7) gauss·pixel^{-1} is a large scale gradient, pre-flare parameters are shown in brackets**.** Average field in the vicinity of SPIL (±10 SDO pixels) seems to be quite regular. Its variation with transition from quiet to pre-flare conditions is within the 95% confidence interval. Parameters B and C of the fitting function (Equation (11)) show some increasing of the gradient before the flare but accuracy of the fit is questionable due to high uncertainty of the average.

Strong flux (up to 10^3 gauss) pixels appear regularly on the SPIL itself and their number increases with transition from quiet to pre-flare conditions (Figure 5). The Kolmogorov - Smirnov nonparametric two-sample statistical test shows some different distributions of the magnetic fields which form the SPIL for pre-flare and quiet conditions (Figure 5). SPIL with a 50 gauss threshold rejects the null-hypotheses that the data come from the same distribution with 99.99% significance, whereas SPIL with a 100 Gauss threshold rejects this hypotheses with 90% significance.

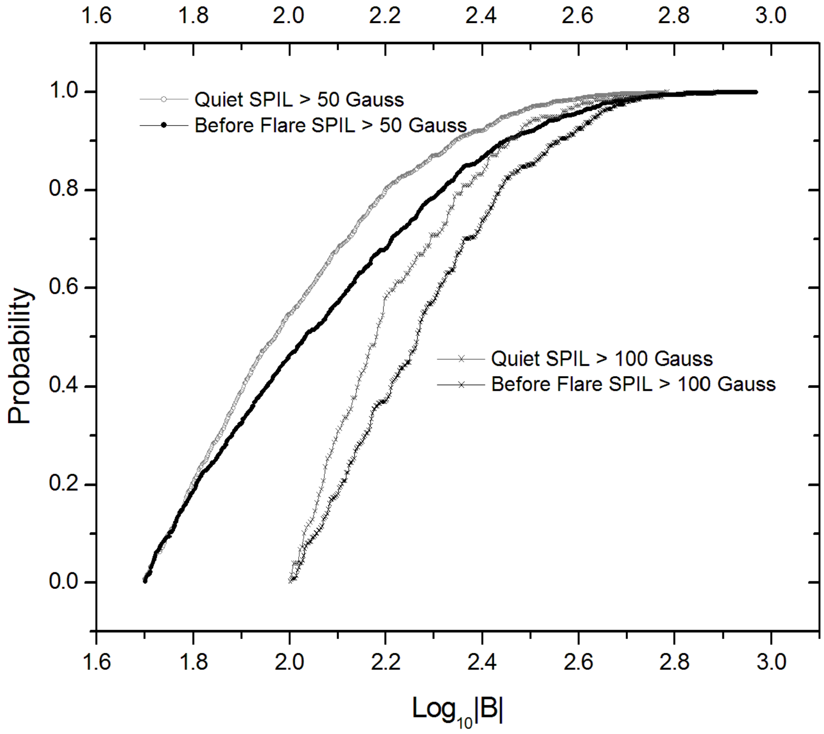

Figure 5. Cumulative probability of the magnetic fields which form the SPIL for quiet (11:00) and pre-flare (17:20) conditions. Magnetic field of opposite polarity pixels across the SPIL is taken without sign. Rich (50 Gauss threshold SPIL) and rare (100 Gauss threshold) statistics are shown with hysteresis-type curves.

We can see from Figure 5 that the distribution shifts to stronger magnetic fields, which is consistent with the known fact of the increasing of the total unsigned magnetic flux before flare.

Conclusions

We propose an effective algorithm of identification of strong polarity-inversion lines from SDO line-of-sight magnetogram without smoothing. An extended version of the algorithm allows calculating the profile of the magnetic field connecting regions of high magnetic fluxes of opposite polarity through the strong polarity-inversion line. This profile has a regular shape and is fitted with an analytical function.

Testing these algorithms we provide a pilot study of the AR 11158 X-class flare and show that calculated parameters (GWILL flux and length-per-object) tend to grow before flare consistently with previous findings for SOHO magnetograms treated with more complex algorithms.

Acknowledgements

I thank the SDO team for producing high-quality data and providing open access for these at http://hmi.stanford.edu/ . I also thank the anonymous referee for helpful comments. The work is supported by grants: Program of the Presidium of Russian Academy of Science N 16, Russian Fund of Basic Research N 10-02-00391-a, 11-02-00755-a, Scientific School SC-3645.2010.2.

References

Barnes, G., Leka, K.D.: 2006, *Astrophys. J.*, **646**, 1303.

Barnes, G., Leka, K.D.: 2008, *Astrophys. J. Lett.*, **688**, L107.

Barnes, G., Longscope, D.W., Leka, K.D.: 2005, *Astrophys. J.*, **629**, 561.

Benkhalil, A., Zharkova, V. V., Zharkov, S., Ipson, S.: 2006, *Solar Phys.* **235**, 87.

Cui, Y., Li, R., Wang, H., He, H.: 2007, *Solar Phys.* **242**, 1.

Cui, Y.M., Li, R., Zhang, L.Y., He, Y.L., Wang, H.N.: 2006, *Solar Phys.* **237**, 45.

Falconer, D.A, Moore, R.L., Gary, G.A.: 2008, *Astrophys. J.*, **689**, 1433.

Falconer, D.A., Moore, R.L., Gary, G.A.: 2003, *J. Geophys. Res.*, **108,** 1380.

Gary, G.A., Moore, R.L., Hagyard, M.J., Haisch, B.M.: 1987 *Astrophys. J.*, **314**, 782.

Georgoulis, M.K., Rust, D.M.: 2007, *Astrophys. J. Lett.*, **661**, L109.

Gorbachev, V.S., Somov, B.B.: 1988, *Solar Phys.* **117**, 77.

Leka, K.D., Barnes, G.: 2003a, *Astrophys. J.*, **595**, 1277.

Leka, K.D., Barnes, G.: 2003b, *Astrophys. J.*, **595**, 1296.

Martens, P.C.H., Attrill, G.D.R., Davey, A.R., Engell, A., Farid, S., Grigis, P.C., Kasper, J., Korreck, K., Saar, S.H., Savcheva, A. *et al.* 2011, *Solar Phys.* DOI: 10.1007/s11207-010-9697-y

Mason, J.P. and Hoeksema, J.T.: 2010 *Astrophys. J.*, **723**, 634.

Moor, R.L., Sterling, A.C.: 2001, *Astrophys. J.*, **552**, 833.

Priest, E.R., Forbes, T.G. : 2002, *Astron. Astrophys. Rev.* **10**, 313.

Ronse, C., Serra, J.: 2001, *Fundamenta Informaticae* **46**, 1.

Schrijver, C. J.: 2007, *Astrophys. J. Lett.*, **655**, L117.

Schrijver, C. J.: 2009, *Adv. Space Res.*,**43**,739.

Serra, J.,1998: *J. Math. Imaging Vision*, **9**, 231.

Shibata K.: 1998, *Astrophys. Space Sci.*, **264**, 129.

Sterling, A.C., Harra, L. K., Moore, R.L.: 2007, *Astrophys. J.*, **669**, 1359.

Wang, H., Spirock, T. J., Qiu, J., Ji, H., Yurchyshyn V., Moon, Y.-J. , Denker, C., Goode, P. R.: 2002 *Astrophys. J.*, **576**, 497.

Wang, Y. and J. Zhang: 2008. *Astrophys. J.*, **680**, 1516.